PHYSICAL REVIEW D **103,** 042008 (2021)

Higher-order Hermite-Gauss modes for gravitational waves detection

Stefan Ast,[*] Sibilla Di Pace,[†] Jacques Millo,[‡] Mikhaël Pichot, Margherita Turconi,
Nelson Christensen, and Walid Chaibi[§]
ARTEMIS, Université Côte d'Azur, CNRS and Observatoire de la Côte d'Azur,
Boulevard de l'Observatoire F-06304 Nice, France

(Received 4 February 2019; revised 7 March 2020; accepted 7 January 2021; published 16 February 2021)

As part of the research on thermal noise reduction in gravitational-wave detectors, we experimentally demonstrate the conversion of a fundamental TEM_{00} laser mode at 1064 nm to higher-order Hermite-Gaussian modes (HG) of arbitrary order via a commercially available liquid crystal spatial light modulator. We particularly studied the $\mathrm{HG}_{5,5}/\mathrm{HG}_{10,10}/\mathrm{HG}_{15,15}$ modes. A two-mirror plano-spherical cavity filters the higher-order modes spatially. We analyze the cleaned modes via a three-mirror diagnosis cavity and measure a mode purity of 96/93/78% and a conversion efficiency of 6.6%/3.7%/1.7%, respectively. A full set of simulations and mathematical proofs are also presented which shows that (i) Hermite-Gauss modes resonate in a two-mirror cavity provided mirrors are properly angled with respect to the impinging mode, and (ii) Hermite-Gauss modes resonate in triangular cavities. Hence, higher-order Hermite-Gauss modes are compatible with ground-based gravitational-wave detectors' architecture and can be employed for the mitigation of mirror thermal noise for the third generation Einstein Telescope or Cosmic Explorer.

DOI: 10.1103/PhysRevD.103.042008

I. INTRODUCTION

Lasers used for high-precision experiments typically generate an output beam in the fundamental TEM_{00} mode. Their operation at higher-order Hermite-Gauss ($\mathrm{HG}_{m,n}$) or axisymmetric Laguerre-Gaussian ($\mathrm{ALG}_{p,l}$) modes suffers from low lasing efficiency due to diffraction losses and a less stable output mode [1] ($\{m, n\}$ and $\{p, l\}$ represents the HG and ALG modes orders, respectively, using the notations of [1]). However, higher-order modes are beneficial in metrology experiments using optical cavities or laser interferometers that are fundamentally limited by thermally induced mirror surface motions that reduce the length sensing sensitivity [2]. More specifically, reference cavities used for the frequency stabilization of the optical oscillator in optical clocks are currently limited by thermal noise of the highly reflective mirror coatings with a fractional frequency instability of 4×10^{-17} in 1 s [3]. Second generation of gravitational waves (GW) detectors (Advanced LIGO [4], Advanced Virgo [5], KAGRA [6]) are also limited by the coatings' thermal noise in the frequency band of 50–200 Hz with $h = 3 \times 10^{-24}$ $[1/\sqrt{\mathrm{Hz}}]$ at 100 Hz for Advanced LIGO [7–9]. With the reduction of quantum noise, third generation of GW detectors are foreseen to be limited by mirrors thermal noise at a level of 3×10^{-25} $[1/\sqrt{\mathrm{Hz}}]$ at 100 Hz for the high frequency detector of the Einstein Telescope [9,10] and 3×10^{-25} $[1/\sqrt{\mathrm{Hz}}]$ at 20 Hz for the Cosmic Explorer [11,12]. One way to address this problem is with cryogenically cooled mirrors [13], and this is presently being tested with KAGRA [14]. In addition, the negative effect of thermal noise can be mitigated by using a spatially broader intensity profile for the laser beam in comparison to the fundamental TEM_{00} mode. This results in a higher averaging over the mirror surface for the same cavity characteristics [15–19]. This can be achieved by using higher-order modes whose efficiency increases with the total mode order N_T ($N_T = m + n$ for $\mathrm{HG}_{m,n}$ modes and $N_T = 2l + p$ for $\mathrm{ALG}_{p,l}$ modes) [20]. Higher-order Laguerre-Gauss modes were the first to be suggested for ground based GW detectors [8,21] and this idea was extended for reference cavities related to optical clocks [22]. A reduction of thermal noise was recently demonstrated in a 10-cm ULE glass reference cavity using the $\mathrm{HG}_{0,2}$ mode [23].

For GW detection, the higher-order modes must be high power (efficiently generated), pure, and robust with respect to mirrors defects and aberrations. The $\mathrm{ALG}_{3,3}$ mode has been the object of several experimental investigations in this context [24–33] was demonstrated to be incompatible with GW detectors due to mirror aberrations in the current state of the art of mirror's manufacturing techniques. In this paper we investigate the conversion of the fundamental

---

[*] stefan.ast@aei.mpg.de; Present Address: Max Planck Institute for Gravitational Physics (Albert Einstein Institute) and Institute for Gravitational Physics of Leibniz Universität Hannover, D-30167 Hannover, Germany

[†] Present Address: Università degli Studi di Roma La Sapienza & INFN Sezione di Roma1, Rome, Italy

[‡] Present Address: Institut FEMTO-ST, 25030 Besançon, France

[§] chaibi@oca.eu

HG_{00} mode at 1064 nm into highly pure $HG_{m,n}$ modes with orders never reached up to now and demonstrate their compatibility with both linear and triangular cavities used in GW detectors. HG modes are likely to represent intracavity modes thanks to their insensitivity to mirrors' astigmatism in certain conditions or to the cavity architecture itself. The application of these modes for thermal noise reduction could be important for third generation GW detectors, such as Einstein Telescope [9,10] and Cosmic Explorer [11,12].

The remainder of this paper is organized as follows. In Sec. II we compare the utility of HG modes in comparison to ALG modes. Section II presents that results of simulations of HG modes in Virgo-like cavities. The effects of imperfect mirror orientations as discussed in Sec. IV. The experimental generation of HG and measurements of their characteristics are given in Sec. V. The concluding comments are in Sec. VII, while an Appendix presents more supporting theoretical material.

II. ALG VERSUS HG

Thermal noise at low frequencies in optical cavities operating with axisymmetric ALG modes is computed in [21,34] using the Bondu-Hello-Vinet (BHV) technique [35] (extended in [36]). This calculation is based on Levin's theory [37] and is applied on finite mirrors. HG modes' related thermal noise was computed analytically in [20] only for infinite mirrors. Based on the latter reference, we compare in Table I the mitigation efficiency of thermal noise for the $ALG_{5,5}$ mode, a frequent example in theoretical computations [21,34,38], the $ALG_{3,3}$ mode, and the HG modes $HG_{5,5}$, $HG_{10,10}$. Coating Brownian thermal noise is currently limiting both reference cavities and GW detectors, whereas the thermoelastic noise limit, which undergoes similar reduction factors, lies below that and is not considered here. ALG modes are more efficient to mitigate thermal noise for equivalent clipping losses. However, it was found that the ALG modes pose strong requirements on the mirror surface quality since they exhibit a mode pseudodegeneracy [31] that greatly decreases their coupling efficiency to linear cavities. Residual astigmatism of the mirrors turns out to be the main defect responsible for the intracavity mode degradation [27,32] and its thermal compensation was demonstrated to improve the mode quality [28]. Astigmatism also prevents ALG modes from resonating in a four-mirror premode cleaner unless they are in a nonplanar configuration [33]. Note that ALG modes do not resonate in triangular cavities [26], which are largely used in GW detectors.

TABLE I. Calculated thermal noise limit reduction factor for higher-order modes with respect to the Gaussian mode for both substrate and coatings. a represents the mirror radius and w designates the beam radius. The ratio a/w considered here corresponds to a clipping loss of 1 ppm. These calculations are based on [20].

	Order	Substrate	Coatings	a/w
HG	5,5	0.576	0.493	4.379
	10,10	0.491	0.392	5.513
ALG	3,3	0.559	0.378	3.313
	5,5	0.496	0.310	4.968

In a two-mirror cavity, the HG pseudodegeneracy is strictly related to the coupling between HG modes of the same total order during the reflection on mirrors, i.e., between $HG_{m,n}$ and $HG_{m+q,n-q}$ (the case of three-mirror cavities will be described further in this paper). As stated in [27,32], astigmatism represents the main contribution to the mirrors distortions and, in the specific case of GW detector mirrors, it mainly couples the impinging mode to the two adjacent ones, i.e., $q = \pm 1$. Thanks to symmetry considerations and whatever the astigmatism radial profile is, this coupling is canceled when the astigmatism profile is aligned on either one of the impinging two mode axes. Hence, one just needs to angle the mirror around the beam axis adequately to minimize the total coupling into HG modes of equal total order N_T. The ALG mode coupling remains unaffected by mirror angling because of their axisymmetry. The case of nonaxisymmetric ALG modes needs to be carefully studied. To confirm these assertions, FFT-based simulations using the software DarkF [39,40] on a $\simeq$1 km cavity using the measured map of an Advanced Virgo mirror are described in the next section. Right after, a mathematical proof is presented for the specific case of the $HG_{5,5}$ mode.

III. DARKF SIMULATIONS OF HG MODES IN A VIRGO-LIKE CAVITY

We present here the DarkF [39,40] simulations of a 1021 m plano-concave cavity with a finesse $F = 1000$. The input mirror is plane and has a transmission $T = 3137$ ppm. Its diameter is 35 cm. The end mirror has an identical transmission and has a radius of curvature $R = 1179$ m. Hence, the g factor of the cavity is $g \simeq 0.13$, the cavity mode waist falls on the input mirror with a beam radius $w_0 \simeq 1.17$ cm and the beam radius on the end mirror is $w_1 \simeq 3.19$ cm for a laser wavelength $\lambda = 1064$ nm. The theoretical power enhancement factor (PEF) is $F/\pi \simeq 318$. These features were chosen in order to keep identical mirrors, similar clipping losses as a $HG_{0,0}$ mode in a 3 km cavity and the same stability, i.e., the same g factor, as for Virgo. A 3 km cavity would have required the use of larger mirrors for which aberration maps are unavailable.

The simulations presented below were conducted considering the input mirror with a perfect surface, whereas the end mirror presents the distortions displayed on Fig. 1 that represent a Virgo-like mirror surface residual when piston, tilts, and curvature are subtracted for the Virgo intracavity beam. The surface error considered here is 0.5 nm rms

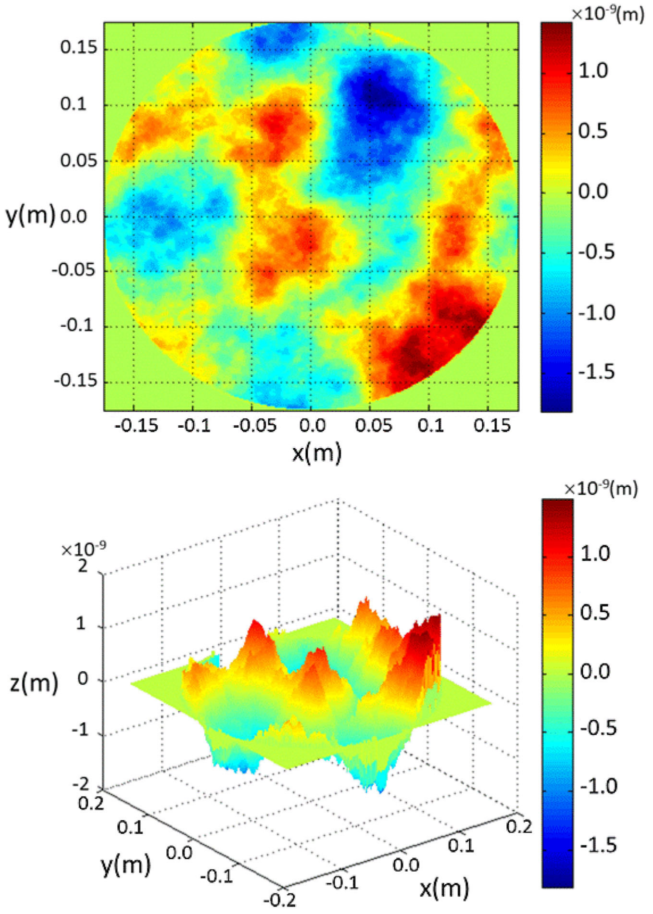

FIG. 1. Generated coated mirror map by the software OSCAR [41,42] based on the mirror's characteristics of the Advanced Virgo project. The figure represent the mirror's distortion when piston, tilts and curvature are subtracted. The residual distortion is 0.5 nm rms. Courtesy of Jérôme Degallaix

corresponding to the requirements of the Advanced Virgo project.

DarkF is a software based on an FFT algorithm to compute the Fresnel propagation of the laser beam from one mirror to the other. The injected beams used here are $\mathrm{ALG}_{3,3}$, $\mathrm{ALG}_{5,5}$, $\mathrm{HG}_{5,5}$, and $\mathrm{HG}_{10,10}$, whose intensity distributions are represented in Fig. 2.

The end mirror is angled around the optical axis in order to maximize the mode matching into the cavity. Obviously, this procedure has no effect on the ALG modes coupling efficiency. The power enhancement factor (PEF), the mode matching and the round trip losses (RTL) are given in Table II for the optimum angles, and show $\mathrm{ALG}_{3,3}$ and $\mathrm{ALG}_{5,5}$ mode coupling efficiencies do not exceed 70%. On the other hand, the $\mathrm{HG}_{5,5}$ and $\mathrm{HG}_{10,10}$ mode coupling increases from 77% to 99% and from 62% to 96%, respectively, when one rotates the mirrors by the correct angle. PEF also increases accordingly. Note that the optimum angles for $\mathrm{HG}_{5,5}$ and $\mathrm{HG}_{10,10}$ are different since the latter explores a wider surface of the mirror than the former thus showing that aberration effects are mode dependent. The simulated intensity profiles of the intracavity modes are displayed in Fig. 3. A clear improvement of the HG modes profiles appears between the 0° angle and optimum angles for which distortions are no more observed. This renders higher-order HG modes as promising candidates for applications in GW detectors although they provide a slightly smaller mitigation effect of thermal noise. A full explanation of these results is presented in the next section.

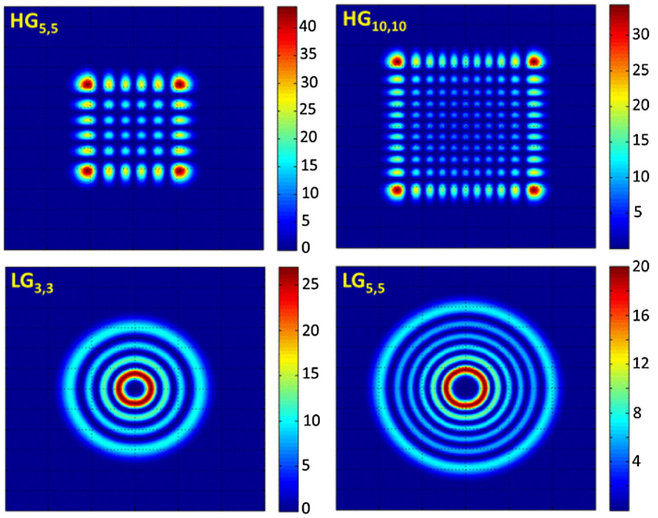

FIG. 2. Simulated intensity distribution of the high order modes which are injected into the cavity.

IV. EFFECT OF THE IMPERFECT MIRROR ORIENTATION

In this section, we describe how the mirror distortion couples between HG modes of the same N_T that is responsible for the pseudodegeneracy effect. This is to explain the results of the previous section. In the general case, let $\psi_0(x,y)$ be the mode impinging on the mirror, (x,y) being the transverse spatial coordinates. In the paraxial approximation, the reflected beam is written as

$$\psi_r(x,y) = e^{i2kz(x,y)}\psi_0(x,y), \tag{1}$$

where $k = 2\pi/\lambda$ represents the wave vector. When the incident beam ψ_0 is a $\mathrm{HG}_{m,n}$ mode, we are interested in the contribution of each $\mathrm{HG}_{m+q,n-q}(-\max(m,n)\leq q\leq \min(m,n))$ to ψ_r. These contributions are given by the coefficient γ_q defined as

$$\begin{aligned}\gamma_q &= \int \psi_r(x,y)\mathrm{HG}^*_{m+q,n-q}(x,y)dxdy,\\ &\simeq \delta_{q,0} + i2k\\ &\quad\times \int \mathrm{HG}_{m,n}(x,y)z(x,y)\mathrm{HG}^*_{m+q,n-q}(x,y)dxdy,\end{aligned} \tag{2}$$

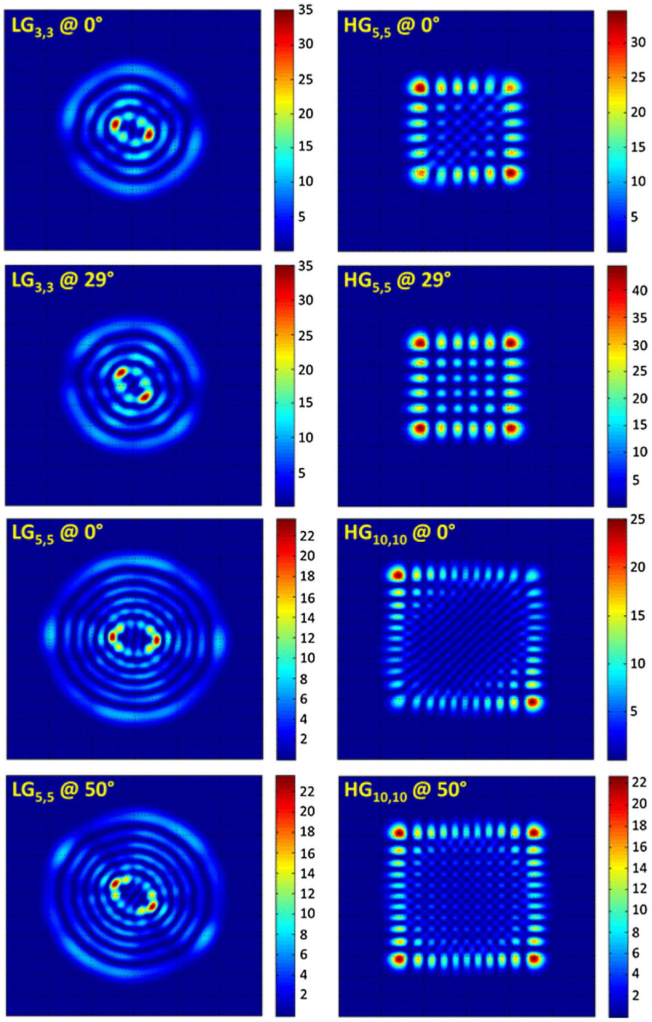

FIG. 3. Simulated intensity profiles of intracavity modes for different angles.

where * designates the complex conjugate and the integral is performed on the mirror surface. The last approximation is valid for distortions much smaller than the laser wavelength, i.e., $z \ll \lambda$. Hence, γ_q represents the coupling of the injected mode into other modes of the same total order N_T. In the following, we study the specific case of the $HG_{5,5}$ mode and the corresponding coupling coefficient γ_q when reflected on the mirror as shown in Fig. 1. We also define Γ_q as the contribution of the $HG_{5+q,5-q}$ to the mode of the cavity studied in Sec. II defined by

$$\Gamma_q = \int \psi_{\mathrm{int}}(x,y)\mathrm{HG}^*_{m+q,n-q}(x,y)dxdy,$$

where ψ_{int} designates the intracavity mode. In Table III, we display both absolute values of γ_q and Γ_q, and two points stand out: (i) the contributions of $HG_{4,6}$ and $HG_{6,4}$, i.e., $q \pm 1$, are dominant; (ii) the orientation of the mirror by the optimum angle 29° reduces both the contribution $q \pm 1$ while keeping the other contributions $|q| > 1$ negligible. In the following, we present an analysis based on Zernicke polynomials formalism, which explains the two former points.

TABLE II. Coupling efficiency of considered HG and ALG modes for different end mirrors angles. The coupling efficiency of ALG modes does not depend on the angle.

	Angle (°)	PEF	Matching (%)	RTL (ppm)
$ALG_{3,3}$		218	68	0.27
$ALG_{5,5}$		207	65	0.3
$HG_{5,5}$	0	246	77	0.3
	29	315	99	0.56
$HG_{10,10}$	0	197	62	1.4
	50	305	96	3

A. The Zernike polynomials

Zernike polynomials [43] are a set of continuous and orthogonal 2D functions over the unit circle. They are noted by $\mathcal{Z}_N^M$. They are defined by two integer indices (N, M) satisfying the conditions $N \geq 0$, $|M| \leq N$, and (N, M), which have the same parity. In polar coordinates (r, θ), $\mathcal{Z}_N^M$ is written as

$$\mathcal{Z}_N^M(r,\theta) = \mathcal{R}_N^M(r)\cos(M\theta) \quad \text{for } M \geq 0$$
$$\mathcal{Z}_N^M(r,\theta) = \mathcal{R}_N^M(r)\sin(M\theta) \quad \text{for } M < 0$$

Normalized Zernike polynomials satisfy the orthonormality condition:

$$\int_0^1 rdr \int_0^{2\pi} d\theta \mathcal{Z}_N^M(r,\theta) \times \mathcal{Z}_{N'}^{M'}(r,\theta) = \delta_{NN'}\delta_{MM'}. \qquad (3)$$

TABLE III. Coupling coefficients between $HG_{5,5}$ and $HG_{5+q,5-q}$ for 0° and 29° orientation angles. γ corresponds to coupling after a single reflection; Γ corresponds to the coupling within the cavity. Couplings at $q = \pm 1$ are dominant at 0° and are significantly reduced at 29°. The rest of the coupling coefficients remain negligible.

q	$\lvert\gamma_q\rvert$ for 0°	$\lvert\gamma_q\rvert$ for 29°	$\lvert\Gamma_q\rvert$ for 0°	$\lvert\Gamma_q\rvert$ for 29°
−5	3.1×10^{-6}	2.9×10^{-5}	5.8×10^{-4}	2.4×10^{-4}
−4	5.4×10^{-5}	6.1×10^{-6}	4.1×10^{-4}	7.7×10^{-4}
−3	2.3×10^{-4}	1.9×10^{-4}	6.3×10^{-3}	2.2×10^{-4}
−2	4.6×10^{-4}	3.7×10^{-5}	2.5×10^{-2}	6.3×10^{-4}
−1	1.2×10^{-3}	7.8×10^{-5}	1.1×10^{-1}	1.1×10^{-4}
0	$1 - 2.0 \times 10^{-5}$	$1 - 1.9 \times 10^{-5}$	7.0×10^{-1}	9.9×10^{-1}
1	1.3×10^{-3}	5.5×10^{-5}	1.2×10^{-1}	3.1×10^{-3}
2	2.5×10^{-4}	8.6×10^{-5}	2.2×10^{-2}	8.8×10^{-4}
3	2.5×10^{-5}	2.6×10^{-4}	9.8×10^{-3}	3.0×10^{-5}
4	6.0×10^{-6}	1.7×10^{-5}	2.5×10^{-3}	3.3×10^{-5}
5	6.1×10^{-5}	1.3×10^{-5}	6.7×10^{-4}	8.1×10^{-5}

For a mirror of radius R, we infer a set of orthonormal functions based on the Zernike polynomials defined by

$$Z_N^M(r,\theta) = \mathscr{Z}_N^M\left(\frac{r}{R},\theta\right). \tag{4}$$

The mirror distortions $z(r,\theta)$ displayed in Fig. 1 are then decomposed in $(Z_N^M(r,\theta))_{N,M}$ under

$$z(r,\theta) = \sum_{N,M} c_{N,M} \times Z_N^M(r,\theta) \tag{5}$$

with,

$$c_{N,M} = \frac{1}{R^2}\int_{\text{mirror}} z(r,\theta) Z_N^M(r,\theta) r dr d\theta. \tag{6}$$

Figure 4 shows the result of the decomposition on the Zernike polynomials set up to the order $N_{\max} = 20$, which is to be compared with Fig. 1. The mirror distortion rms value is reproduced with an accuracy better than 2%. The following analysis is based on this decomposition.

B. Lemmas on the HG coupling with Zernike polynomials

In this subsection we address the coupling between the two degenerate modes $\mathrm{HG}_{5,5}$ and $\mathrm{HG}_{5+q,5-q} (q \neq 0)$ thanks to a single Zernike polynomial Z_N^M. For $q \neq 0$, this coupling is given by the following coefficient:

$$\gamma_q^{N,M} = i2k \int \mathrm{HG}_{5,5}(x,y) Z_N^M(x,y) \mathrm{HG}^*_{5+q,5-q}(x,y) dx dy. \tag{7}$$

The following lemmas will be used in the next sections. Proofs can be found in Appendix A.

(i) Lemma 1: for $N = 0$, $\gamma_q^{0,0} = 0$.
(ii) Lemma 2: for N odd, $\gamma_q^{N,M} = 0$.
(iii) Lemma 3: for N even, $\gamma_{q=\text{odd}}^{N,M\geq 0} = 0$ and $\gamma_{q=\text{even}}^{N,M<0} = 0$.
(iv) Lemma 4: for N even, $\gamma_{-q}^{N,M} = (-1)^{1+M/2} \times \gamma_q^{N,M}$ for q odd and $M < 0$ and $\gamma_{-q}^{N,M} = (-1)^{M/2} \times \gamma_q^{N,M}$ for q even and $M < 0$.
(v) Lemma 5: for N even and $N < |2q|$, $\gamma_q^{N,M} = 0$.

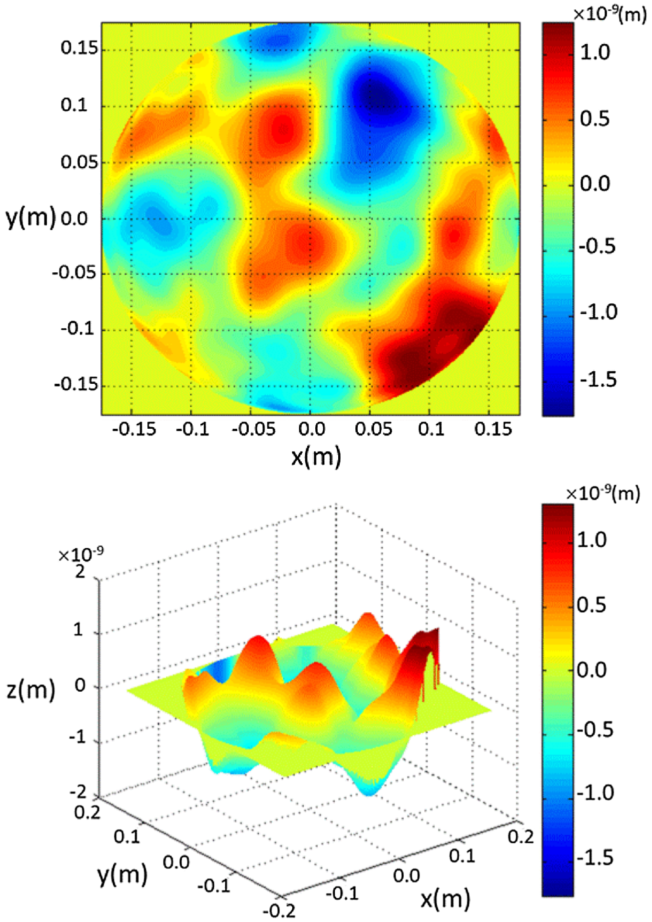

FIG. 4. Mirror map reconstitution with Zernike polynomials up to $N = 20$, to be compared with the map measurement in Fig. 1. The resulting rms value is equal to the original value within 2%.

C. Mirror power spectral density contributions to HG mode coupling

In this subsection, we show that on average, the $\mathrm{HG}_{5,5}$ mainly couples to $\mathrm{HG}_{5+q,5-q}$ modes for $q = \pm 1$. The proofs below combine the mirrors 2D isotropic power spectral density (PSD) [44] and the Zernike polynomial formalism at the same time. In polar coordinates, the mirror PSD is defined as [44,45]

$$\mathrm{PSD}(\kappa,\phi) \simeq \frac{1}{\pi R^2}\left\langle \left| \int_0^R \int_0^{2\pi} e^{i2\kappa r\cos(\theta-\phi)} z(r,\theta) r dr \theta \right|^2 \right\rangle, \tag{8}$$

where $\langle\rangle$ stands for an average over an important number of mirrors. In practice, the PSD is not accessible due to the difficulty to compute this average. The 2D isotropic PSD defined by

$$\mathrm{PSD}_{\text{2-D}}(\kappa) = \frac{1}{2\pi}\int_0^{2\pi} \mathrm{PSD}(\kappa,\phi) d\phi \tag{9}$$

represents the average over the angle ϕ and thus is more accessible since a single mirror offers enough data to compute the average. Now, we address the contribution of each Zernike polynomial to the 2D isotropic PSD. To that aim, we inject the decomposition of the mirror distortions on the set of Zernike polynomials and we obtain this:

$$\mathrm{PSD}_{\text{2-D}}(\kappa) \simeq \frac{1}{\pi R^2}\sum_{N,M}\left\langle\left|c_{N,M}\int_0^R\int_0^{2\pi} e^{i2\kappa r\cos(\theta-\phi)} Z_N^M(r,\theta)\,r dr d\theta\right|^2\right\rangle, \tag{10}$$

where henceforth $\langle\rangle$ also includes an average over the angle ϕ. The last equation involves the 2D Fourier transform $\tilde{Z}_N^M$ of Zernike polynomials, which is given by

$$M \geq 0 \quad \tilde{Z}_N^M(\kappa,\phi) = 2\pi R^2 i^N \frac{J_{N+1}(2\pi\kappa R)}{2\pi\kappa R}\cos(M\phi),$$

$$M < 0 \quad \tilde{Z}_N^M(\kappa,\phi) = 2\pi R^2 i^N \frac{J_{N+1}(2\pi\kappa R)}{2\pi\kappa R}\sin(M\phi).$$

Because of the averaging over ϕ, Eq. (10) simplifies to

$$\mathrm{PSD}_{\text{2-D}}(\kappa) \simeq 2\pi R^2 \sum_N \zeta_N(2\pi\kappa R)\sum_M \langle |c_{N,M}|^2\rangle, \tag{11}$$

where

$$\zeta_N(\xi) = \left(\frac{J_{N+1}(\xi)}{\xi}\right)^2 \quad J_l\text{: Bessel function of order } l. \tag{12}$$

The function $\zeta_l(\xi)$ admits its maximum value around $\mu_l \simeq 1.1l + 1.6$, and decreases rapidly around the corresponding peak. With a rough approximation, we simulate $\zeta_l(\xi)$ as a gate function of height μ_l and a width $\Delta_l \simeq 2.810^{-3}l^2 + 0.14l + 2.4$. Hence, $\mathrm{PSD}_{\mathrm{2D}}$ can be considered as a histogram defined by its values at $\kappa_N = \mu_N/2\pi R$. Defining

$$C_N = \sum_{M=-N}^{N} \langle |c_{N,M}|^2\rangle, \tag{13}$$

where M and N have the same parity, the 2D isotropic PSD becomes

$$\mathrm{PSD}_{\text{2-D}}(\kappa_N) \simeq 2\pi R^2 C_N \Delta_N \left(\frac{J_{N+1}(\mu_N)}{\mu_N}\right)^2. \tag{14}$$

Two points are to be brought into attention here:

(i) For a given N all polynomials Z_N^M are characterized by the same spatial frequency κ_N and have the same weight in the 2D isotropic PSD of the mirrors. Therefore, $\langle |c_{N,M}|^2\rangle = \langle |c_N|^2\rangle$ does not depend on M and we get

$$C_N = (N+1)\langle |c_N|^2\rangle. \tag{15}$$

(ii) The factor C_N characterizes the 2D isotropic PSD with respect to the spatial frequency κ_N.

In the literature 1D PSD are available and simply related to corresponding 2D isotropic PSD by [44]:

$$\mathrm{PSD}_{\mathrm{2D}}(\kappa) = \frac{\mathrm{PSD}_{\mathrm{1D}}(\kappa)}{\kappa} \tag{16}$$

For gravitational-wave detectors mirrors, $\mathrm{PSD}_{\mathrm{1D}}$ has a specific behavior of $1/\kappa^{2.3}$ [46]. Hence, Eq. (14) gives

$$\langle |c_N|^2\rangle \propto \frac{1}{\mu_N^{2.3}(N+1)\Delta_N}\left(\frac{\mu_N}{J_{N+1}(\mu_N)}\right)^2. \tag{17}$$

Now, the global coupling coefficient γ_q defined for $q \neq 0$ by Eq. (2) is written as

$$\gamma_q = \sum_N^M c_{N,M}\gamma_q^{N,M}. \tag{18}$$

The effect of the pseudodegeneracy within the cavity is proportional to $|\gamma_q|^2$ [27]. Since for a given N, all M contributions are equally probable with both positive and negative values, the average effect reduces to

$$\begin{aligned}\langle |\gamma_q|^2\rangle &\propto \sum_N\sum_M |\gamma_q^{N,M}|^2\langle |c_{N,M}|^2\rangle,\\ &\propto \sum_N \langle |c_N|^2\rangle \sum_M |\gamma_q^{N,M}|^2,\end{aligned} \tag{19}$$

and using Eq. (17), one gets

$$\langle |\gamma_q|^2\rangle \propto \sum_N \frac{\mathrm{PSD}_{\mathrm{1D}}(\frac{\mu_N}{2\pi R})\sum_M |\gamma_q^{N,M}|^2}{\mu_N(N+1)\Delta_N}\left(\frac{\mu_N}{J_{N+1}(\mu_N)}\right)^2. \tag{20}$$

Interestingly, Eq. (20) links the average coupling $\langle |\gamma_q|^2\rangle$ to $\mathrm{PSD}_{\mathrm{1D}}$, which is a measurable quantity characterizing the considered mirror. For the specific case of gravitational-wave detector mirrors, one gets

$$\langle |\gamma_q|^2\rangle \propto \sum_N \frac{\sum_M |\gamma_q^{N,M}|^2}{\mu_N^{3.3}(N+1)\Delta_N}\left(\frac{\mu_N}{J_{N+1}(\mu_N)}\right)^2. \tag{21}$$

As stated by Lemmas 1 and 2, only nonzero even N are to be taken into account. Also, for a given q only $N > 2|q|$ are to be computed as shown by Lemma 5. According to Lemma 4, $\langle |\gamma_q|^2\rangle = \langle |\gamma_{-q}|^2\rangle$. So, in Fig. 5, $\langle |\gamma_q|^2\rangle$ is represented for $|q| = 1$ to 5 and its evolution with respect to $N_{\max}$ limit of the sum over N in the case of GW detectors mirrors. It appears that (i) the series over N converges and $N_{\max} = 20$ gives a satisfactory estimation of the coupling. (ii) the coupling into $\mathrm{HG}_{6,4}$ and $\mathrm{HG}_{4,6}$ is dominant with respect to other HG modes. This is in agreement with the numerical values reported in Table III. In the following section, we focus on the coupling into $\mathrm{HG}_{6,4}$ and $\mathrm{HG}_{4,6}$ modes and neglect the rest.

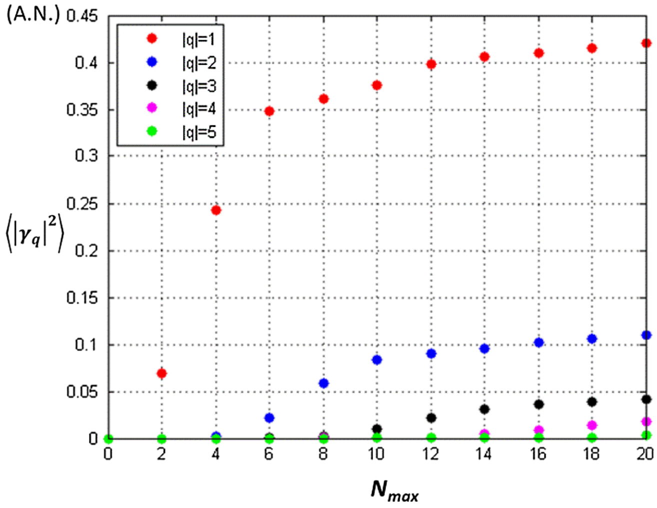

FIG. 5. The calculated evolution of the mean energetic coupling $\langle|\gamma_q|^2\rangle$ between $HG_{5,5}$ and $HG_{5+q,5-q}$ average as a function of the limit $N_{\max}$ of the corresponding sum over N for $1 < |q| \leq 5$. $\langle|\gamma_q|^2\rangle$ converges towards an asymptotic value. $\langle|\gamma_{|q|=1}|^2\rangle$ are dominant.

D. Cancellation of $HG_{6,4}$ and $HG_{4,6}$ couplings by mirror rotation

In this section, we show that the coupling of $HG_{6,4}$ and $HG_{4,6}$ can be severely reduced by rotating the mirror around the optical axis. With respect to the mirror orientation of Fig. 1 for which γ_q and $C_{N,M}$ were used up to now, we consider the rotation angle θ_0 and we define the corresponding coupling coefficient for $q = \pm 1$:

$$\gamma_q(\theta_0) = i2k \int \mathrm{HG}_{m,n}(r,\theta) z(r,\theta-\theta_0) \mathrm{HG}^*_{m+q,n-q}(r,\theta) r dr d\theta, \tag{22}$$

so $\gamma_q = \gamma_q(0)$. According to Lemmas 2 and 3, we are only interested in orders N even and M even and strictly negative. With some algebra, we can show that

$$\gamma_1(\theta_0) = i \sum_{M/2=1}^{\infty} [T_M \cos(M\theta_0) + S_M \sin(M\theta_0)], \tag{23}$$

where

$$T_M = -i \sum_{N/2=M/2}^{\infty} \gamma_1^{N,-M} c_{N,-M} \tag{24}$$

and

$$S_M = -i \sum_{N/2=M/2}^{\infty} \gamma_1^{N,-M} c_{N,M}. \tag{25}$$

According to Lemma 4, likewise we have

$$\gamma_{-1}(\theta_0) = i \sum_{M/2=1}^{\infty} (-1)^{-M/2} [T_M \cos(M\theta_0) + S_M \sin(M\theta_0)]. \tag{26}$$

Hence, the power coupling into $q = \pm 1$ modes is $\beta(\theta_0) = |\gamma_1|^2 + |\gamma_{-1}|^2$, which is given by

$$\beta(\theta_0) = \sum_{\frac{M}{2}=1}^{\infty} \sum_{\frac{M'}{2}=1}^{\infty} (1 + (-1)^{\frac{M+M'}{2}}) \times [T_M \cos(M\theta_0) + S_M \sin(M\theta_0)] \times [T_{M'} \cos(M'\theta_0) + S_{M'} \sin(M'\theta_0)]. \tag{27}$$

In Fig. 6, the values of $|T_M|$ and $|S_M|$ are computed. We infer that $(M = 2, M' = 2)$ have the main contribution, $(M = 2, M' = 4)$ and $(M = 2, M' = 4)$ have zero contribution according to Eq. (27), $(M = 2, M' = 6)$ and $(M = 6, M' = 2)$ contributions are one order of magnitude lower, $(M = 4, M' = 4)$ contributions are two orders of magnitude lower, and so on. Therefore, we can write with 10% accuracy that

$$\beta(\theta_0) \simeq 2[T_M \cos(M\theta_0) + S_M \sin(M\theta_0)]^2 \tag{28}$$

and

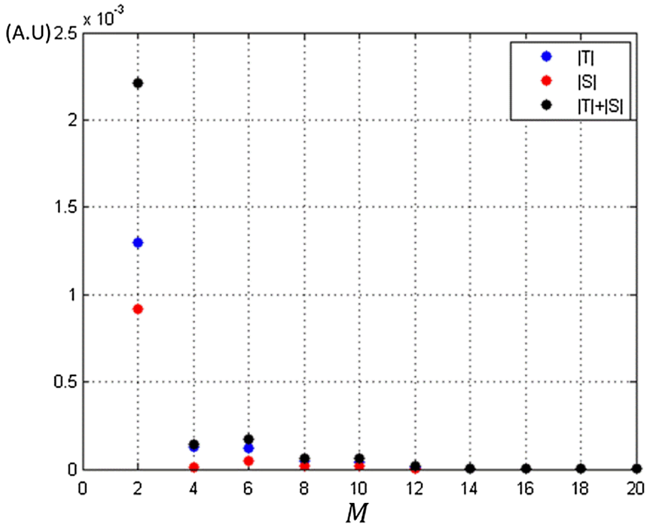

FIG. 6. $|S_M|$, $|T_M|$, and $|S_M| + |T_M|$ as a function of M. $|S_M|$, $|T_M|$, and $|S_M| + |T_M|$ give an order of magnitude of the contribution of the Zernike polynomials for a given M. This figure shows that the contribution $(T,S)_{M=2}$ is at least an order of magnitude higher. Note that the contribution to $|\gamma_1|^2$ are of the form $(T,S)_M \times (T,S)_{M'}$ making the contribution of $(T,S)_M^2$ dominant by at least one order of magnitude.

$$|\gamma_{-1}(\theta_0)| = |\gamma_1(\theta_0)| = |T_2\cos(2\theta_0) + S_2\sin(2\theta_0)|. \quad (29)$$

Note that for $\theta = 0$, $|\gamma_{-1}| = |\gamma_1| = |T_2| \simeq 1.3\times 10^{-3}$, which is in agreement with Table III within 10% accuracy. Interestingly, for $\theta_0 = \Theta_0 = -\frac{1}{2}\arctan(T_2/S_2)$ this approximate coupling γ_1 between $\mathrm{HG}_{5,5}$ and both $\mathrm{HG}_{6,4}$ and $\mathrm{HG}_{4,6}$ cancels out. The order of magnitude of $\gamma_{|q|>1}$ remains unchanged. Θ_0 was computed for different $N_{\max}$ and the result is displayed in Fig. 7. Θ_0 clearly converge towards 27.5°, which is in a good agreement with the value 29° we have reached using DarkF simulations (see Sec. II). Let us recall that the value 29° was obtained while maximizing the coupling of the HG_{55} mode into the cavity. Moreover, these results clearly show that this analysis cannot be reduced to first order astigmatism, i.e., Zernike polynomial $Z_2^{\pm 2}$. Further orders Z_N^{-2} are responsible for the coupling between $\mathrm{HG}_{5,5}$ and $\mathrm{HG}_{6,4}$ or $\mathrm{HG}_{4,6}$. In the following section, we give a physical interpretation of the canceling of the coupling coefficients $\gamma_{\pm 1}$.

E. Physical interpretation

In the frame of the previous approximations, the coupling $\gamma_1(\theta_0) = \gamma_{-1}(\theta_0)$ is of the form

$$\gamma_1(\theta_0) = \left[\sum_{N/2=1}^{\infty} \gamma_1^{N,-2} c_{N,2}\right] \sin(2\theta_0) + \left[\sum_{N/2=1}^{\infty} \gamma_1^{N,-2} c_{N,-2}\right] \cos(2\theta_0). \quad (30)$$

We define the "HG-coupling astigmatism Zernike polynomials" as

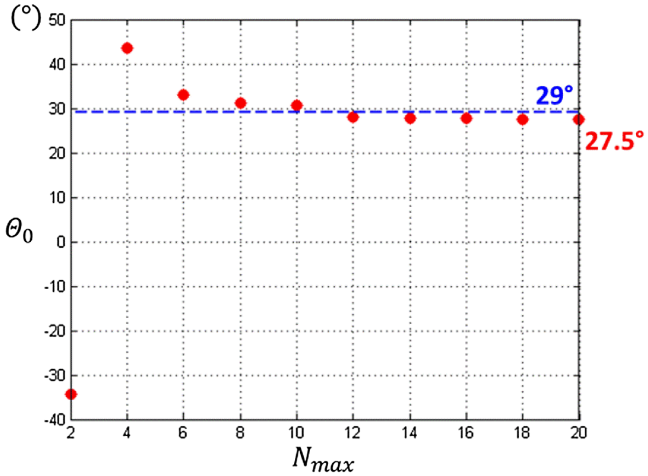

FIG. 7. The rotation angle Θ_0 at which the coupling $|\gamma_{\pm 1}|$ is minimized as a function of $N_{\max}$. The asymptotic value is 27.5° is in agreement with the value 29° computed by FFT simulations. Note that this analysis cannot be reduced to first-order astigmatism $N_{\max} = 2$.

$$\Xi_{M=\pm 2}(r,\theta) = \mathcal{P}(r) \times \begin{cases} \cos(2\theta) & \text{if} \quad M = 2 \\ \sin(2\theta) & \text{if} \quad M = -2 \end{cases}, \quad (31)$$

where

$$\mathcal{P}(r) = \frac{\sum_{N/2=1}^{\infty} \gamma_1^{N,-2} \mathcal{R}_N^2(r/R)}{\sqrt{\sum_{N/2=1}^{\infty} (\gamma_1^{N,-2})^2}}. \quad (32)$$

In Fig. 8, $\Xi_2(r,\theta)$, $\Xi_{-2}(r,\theta)$, and $\mathcal{P}(r)$ are represented. Being linear combinations of Zernike polynomials $Z_N^{\pm 2}(r,\theta)$, to $\Xi_{\pm 2}$ correspond to

(i) The rotated mirror $z(r,\theta-\theta_0)$ projection component:

$$\mathcal{C}_{\Xi,\pm 2}(\theta_0) = \int_{\text{mirror}} z(r,\theta-\theta_0)\Xi_{\pm 2}(r,\theta) r dr d\theta, \quad (33)$$

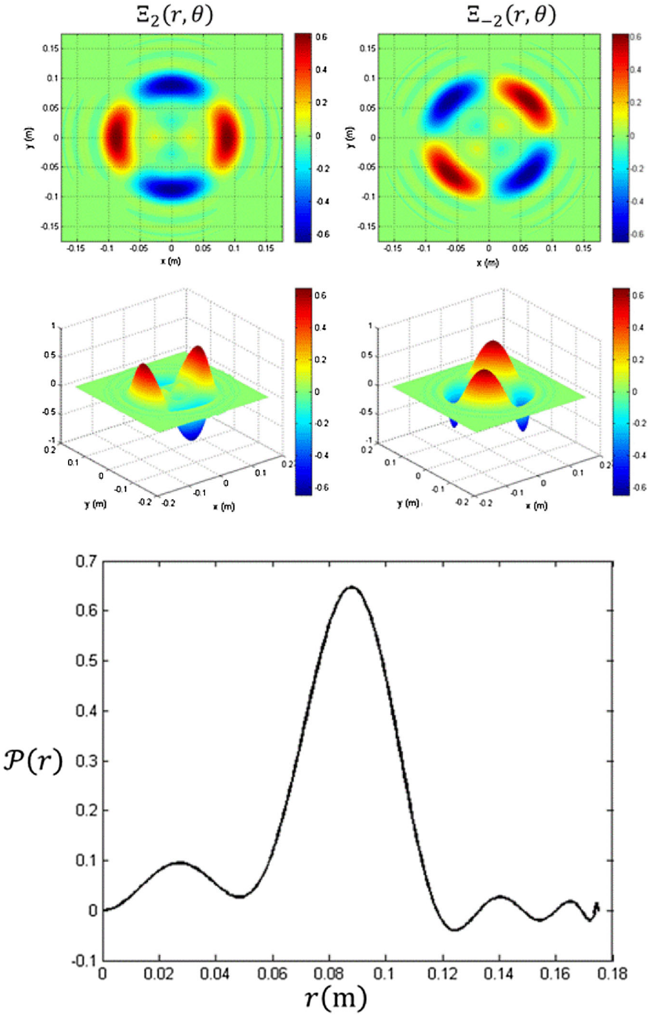

FIG. 8. Top: 2D and 3D representations of the Zernike polynomials $\Xi_{\pm 2}$. Bottom: representation of the polynomial $\mathcal{P}(r)$ for $0 \le r \le R$.

and we have

$$\mathcal{C}_{\Xi,2}(\theta_0) = \mathcal{C}_{\Xi,2}(0)\cos(2\theta_0) - \mathcal{C}_{\Xi,-2}(0)\sin(2\theta_0),$$
$$\mathcal{C}_{\Xi,-2}(\theta_0) = \mathcal{C}_{\Xi,-2}(0)\cos(2\theta_0) + \mathcal{C}_{\Xi,2}(0)\sin(2\theta_0).$$

Obviously this gives $\mathcal{C}_{\Xi,2}(\theta_0)^2 + \mathcal{C}_{\Xi,-2}(\theta_0)^2$ as a constant of θ_0.

(ii) The coupling coefficients between $HG_{5,5}$ and $HG_{6,4}$ (and equally $HG_{4,6}$):

$$\gamma_1^{\Xi,\pm 2} = \gamma_{-1}^{\Xi,\pm 2} = i2k \int HG_{5,5}(r,\theta)\Xi_{\pm 2}(r,\theta)HG^*_{6,4}(r,\theta)rdrd\theta, \tag{34}$$

and obviously we have $\gamma_1^{\Xi,2} = \gamma_{-1}^{\Xi,2} = 0$.

With some algebra, one can demonstrate that

$$\gamma_1(\theta_0) = \gamma_1^{\Xi,-2} \times \mathcal{C}_{\Xi,-2}(\theta_0). \tag{35}$$

Since Θ_0 corresponds to $\mathcal{C}_{\Xi,-2}(\Theta_0) = 0$ and $\gamma_1^{\Xi,2} = 0$, we conclude that with a good approximation, the coupling between $HG_{5,5}$ and $HG_{6,4}$ (and $HG_{4,6}$) is minimized by rotating the mirror around the optical axis by an angle Θ_0, which cancels its projection on Ξ_{-2} and maximizes its projection on Ξ_2, which does not couple the considered HG modes. It clearly appears that these considerations closely depend on the considered impinging mode through the coefficients $\gamma_{\pm 1}$, which explains the difference between optimum angles computed in Sec. II: 29° for $HG_{5,5}$ and 50° for $HG_{10,10}$.

V. EXPERIMENTAL GENERATION OF HG MODES

In our experiment we achieved the conversion of a fundamental TEM_{00} mode to HG modes via the reflection on a commercially available computer addressed liquid crystal phase-only SLM by *Hamamatsu Photonics*. The same technique was used to generate ALG beams [47–54]. The amplitude distribution of the reflected beam is then conserved whereas the phase distribution is exclusively defined by the phase map $\varphi_{SLM}(x, y)$. The HOMs are then obtained out of the field distribution E_{out} in the image focal plane of a Fourier lens. This field distribution is related to the incident beam according to $\mathcal{F}[E_{out}(X, Y)] = |TEM_{00}(x, y)| \exp[i\varphi_{SLM}(x, y)]$ where $\mathcal{F}$ denotes the Fourier transform. Since a $HG_{m,n}$ mode is invariant by $\mathcal{F}$, the last equation shows that a fundamental Gaussian mode cannot be converted into an arbitrary $HG_{m,n}$ mode with 100% efficiency. In [55,56] it is proposed to generate the $HG_{m,n}$ mode in a limited area of the Fourier plane while no condition is imposed on the rest of the plane. The approach is inspired from the Gerchberg-Saxton algorithm [57–59]. It consists of consecutive iterations between the SLM and the Fourier planes using, respectively, the Fourier and inverse Fourier transforms while imposing on each iteration the fundamental mode amplitude on the SLM and the $HG_{m,n}$ mode in the restricted area of the Fourier plane (see Appendix B for further details). Twenty iterations were sufficient to obtain an arbitrary order $HG_{m,n}$ mode within less than 1% error and with a theoretical conversion efficiency spreading up to 45%. The SLM diffraction efficiency decreases with the spatial frequency of the phase map, a nondiffracted light was superimposed to the HG mode in the Fourier plane. A blazed grating was then added to the SLM phase map in order to obtain a free diffraction area. Unwanted light (nondiffracted and diffracted in the free area) was spatially filtered with an iris placed in the Fourier plane. The mode is then filtered by a mode-cleaner cavity.

A simplified schematic picture of the experimental setup is given in Fig. 9. The laser source is a continuous-wave single frequency Nd:YAG nonplanar ring oscillator (NPRO) at 1064 nm. The laser beam is spatially filtered via a single-mode polarization maintaining fiber. A fiber-based electro-optical modulator generates phase modulated sidebands at 100 MHz for a Pound-Drever-Hall [60] cavity stabilization scheme. The generated phase map is then applied to a liquid crystal phase-only SLM type LCOS-SLM X10468 by *Hamamatsu Photonics* having 792 × 600 pixels with a pixel pitch of 20 μm. We used a laser power between 3 mW and 1 W on the SLM. The $HG_{5,5}/HG_{10,10}/HG_{15,15}$ modes are transmitted to a 15 cm long two-mirror planospherical cavity acting as a mode

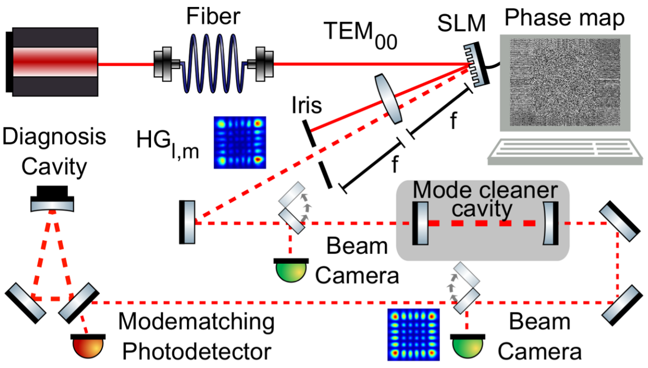

FIG. 9. Simplified scheme of the experimental setup. The fundamental laser mode at 1064 nm is spatially filtered via a single-mode polarization maintaining fiber. A computer generated phase map of the higher-order $HG_{l,m}$ mode is applied to the liquid crystal spatial light modulator (SLM) (top right). An iris separates the higher-order mode from the TEM_{00} mode via a Fourier lens with a focal length f. The higher-order laser beams ($HG_{5,5}/HG_{10,10}/HG_{15,15}$) are spatially filtered via a two-mirror cavity. The mode shape is detected with a beam camera and the mode purity is analyzed with a three-mirror cavity (diagnosis cavity). A custom-made photodetector measures the mode matching of the diagnosis cavity in reflection.

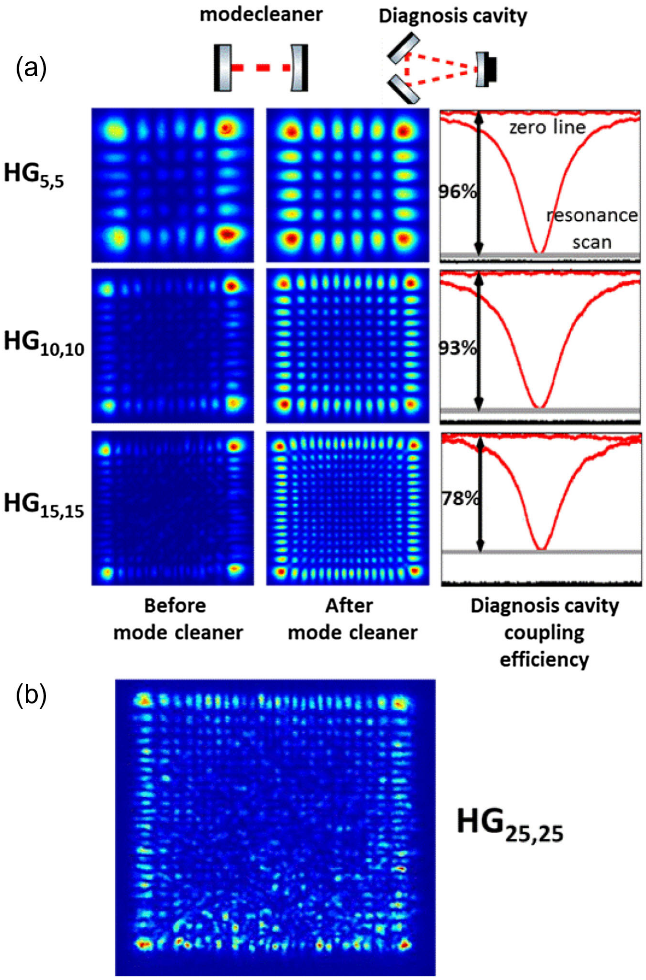

FIG. 10. (a) Intensity profile measurements of the $\mathrm{HG}_{5,5}$ (top), $\mathrm{HG}_{10,10}$ (middle), and $\mathrm{HG}_{15,15}$ (bottom) modes. The mode purity is given by the measurement of the coupling efficiency on the reflection signal of the three-mirror diagnosis cavity. The red resonance curves depict a low amplitude length scan over the diagnosis cavity resonance. (b) Beam camera measurement showing a $\mathrm{HG}_{25,25}$ mode. The picture was taken directly after the generation of the mode without spatial filtering.

cleaner on which the laser is locked via the Pound-Drever-Hall scheme. The mode cleaner cavity finesse is 457 with a free spectral range of 997 MHz. We achieved a mode matching of 62% for the $\mathrm{HG}_{5,5}$ mode, 47% for the $\mathrm{HG}_{10,10}$ mode and 28% for the $\mathrm{HG}_{15,15}$ mode, respectively. Note that the mode cleaner mirrors had to be angled so to obtain qualitatively pure modes at the cavity output.

For high spatial frequency diffraction as is present in our experiment, the SLM expected efficiency from its datasheet is limited to a maximal value of 40%. The iterative algorithm calculated a projection efficiency from the TEM_{00} mode to the $\mathrm{HG}_{5,5}$ of about 28% and to the $\mathrm{HG}_{10,10}/\mathrm{HG}_{15,15}$ modes of about 25%. These values are used to achieve a trade-off between a technically feasible mode size and the SLM's pixel size. Taking into account the mode coupling into the mode cleaner cavity, the total conversion efficiencies are expected to be 6.9% for the $\mathrm{HG}_{5,5}$ mode, 4.7% for the $\mathrm{HG}_{10,10}$ mode and 2.8% for the $\mathrm{HG}_{15,15}$. The experiment achieved a conversion efficiency of, respectively, 6.6%/3.7% and 1.7% for $\mathrm{HG}_{5,5}/\mathrm{HG}_{10,10}/\mathrm{HG}_{15,15}$. For these modes, the differences between measured conversion efficiencies and corresponding expected values are satisfactory. Figure 10(a) displays the intensity profile measurements of the $\mathrm{HG}_{5,5}$, $\mathrm{HG}_{10,10}$, and $\mathrm{HG}_{15,15}$ modes. In addition, we generated a $\mathrm{HG}_{25,25}$ mode to show the possibility of generating arbitrarily HOMs. Its intensity profile right after the Fourier plane is shown in Fig. 10(b).

VI. BEAM PURITY MEASUREMENT

As pointed out by Fulda *et al.* [26], one can inject the considered optical mode into a nondegenerate diagnosis cavity and measure its coupling efficiency in order to quantify its purity. This method was identified to be non ideal to test the purity of ALG modes because the cavity modes themselves are not pure ALG modes. A partial measurement of the ALG mode purity was made by fitting the intensity profile with the corresponding analytical function at some spatial location [24,26], which gives un upper limit to the mode purity since the information on the phase is lost. Unless the mirrors are angled with respect to each other and to the incoming mode as described above, testing HG modes faces the same difficulty. In the following, we show that HG modes purity can be measured using a triangular cavity.

A. HG modes coupling in a triangular cavity

We first consider a linear cavity in which the astigmatism is high enough to lift the degeneracy between modes of constant total order $N_T = m + n$ beyond the cavity bandwidth: this cleans up the cavity mode [61–63] from pseudodegeneracy. In order to confirm this assertion, DarkF simulations were conducted on the same Virgo-like cavity by artificially adding a curvature to the end mirror either along the x or y axis. We then compute the mode behavior while changing the radius of curvature independently along the HG mode axis, namely R_x and R_y in the range [1172 m, 1185 m]. The results of the mode matching are displayed on the top of Fig. 11. On the diagonal, where only residual astigmatism exists, the matching remains below 70% for both $\mathrm{HG}_{5,5}$ and $\mathrm{HG}_{10,10}$. When the additional astigmatism is important enough, the matching exceeds 95%. On the bottom of Fig. 11, the intensity profiles of intracavity modes are displayed for the maximum astigmatism considered here $R_x/R_y \simeq 0.99$.

The degeneracy lifting is even more efficient in the case of a triangular cavity since adjacent modes ($q = \pm 1$) which are dominantly coupled with the injected mode are of opposite symmetry with respect to the latter. Hence, they

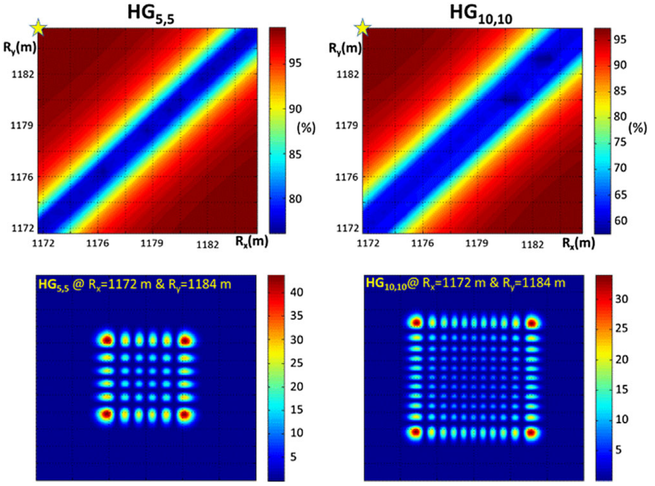

FIG. 11. Top: calculated matching as a function of mirror curvature R_x and R_y. Yellow stars correspond to the astigmatism maximum. Bottom: simulated intensity profiles of the intracavity modes for the astigmatism maximum.

are expelled by half the free spectral range. More generally, this is the case for q odd. $q \geq 2$ even modes for which the coupling with the injected mode turned out to be negligible are expelled by the q times the astigmatism degeneracy lifting. The triangular cavity can then be considered as a HG mode reference.

B. Results and discussion

We analyzed the mode purity via a length tunable three-mirror triangular cavity whose finesse is about 709. Its round trip length is 42.5 cm, resulting in a free spectral range of 706 MHz. The beam impinges on the 50 cm radius of curvature spherical back mirror with an angle of 4°. This makes the astigmatism degeneracy lifting between modes of constant total order N_T and of the same symmetry approximately $q \times 1.75$ times the cavity pole for q even. The mode was detected in transmission of the diagnosis cavity via a *Dataray WincamD* beam camera (512×512 pixels and a pixel size of $9.3 \times 9.3\ \mu\mathrm{m}^2$) while scanning the cavity length. In Fig. 12 the transmitted cavity beams are displayed for different injected modes and they appear to be qualitatively pure HG modes.

The mode matching of the fundamental mode is measured by observing the resonance peak on the reflected signal while the cavity length is being scanned. Special care is taken to collect the whole reflected power on the photodiode. We first matched the fundamental HG$_{0,0}$ to have a reference for the achievable mode matching of the HOMs and the coupling was better than 99%. The mode matching of the HOMs required some slight additional adjustments and revealed a coupling efficiencies of 96%/93%/78% for the HG$_{5,5}$/HG$_{10,10}$/HG$_{15,15}$ modes, as depicted in the right column of Fig. 10(a).

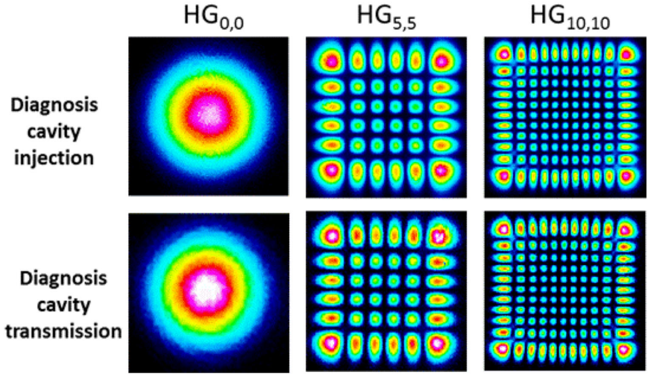

FIG. 12. From the experiment, the comparison between the injected and transmitted beams through the triangular diagnosis cavity for HG$_{0,0}$, HG$_{5,5}$, and HG$_{10,10}$ modes showing that the cavity mode is a true HG mode. Transmitted images are slightly fuzzy because they were taken while the diagnosis cavity is being scanned.

One may wonder what would the purity of these HG modes be when partially measured by the intensity profile method. This procedure was applied to all HG modes we generated, and this purity upper limit ranged from 97% to

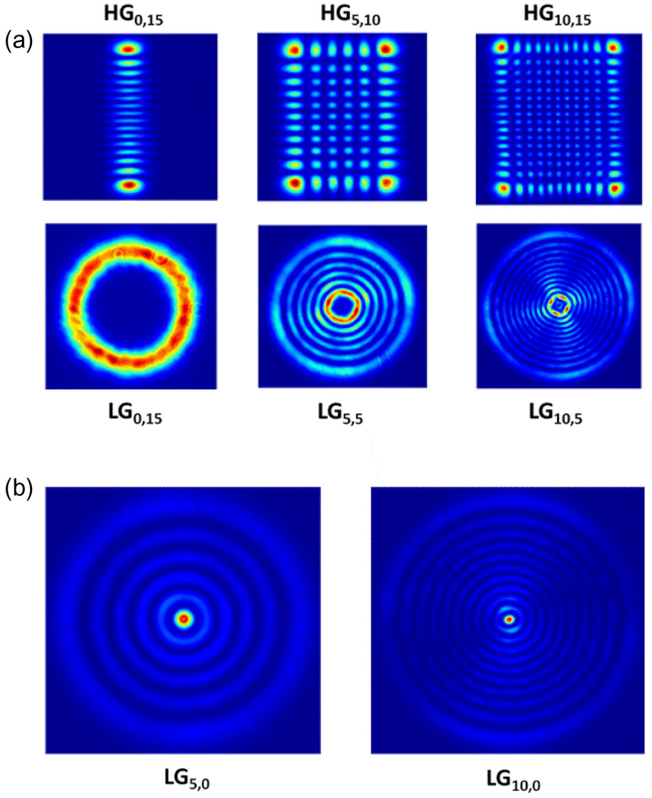

FIG. 13. From the experiment. (a) ALG modes generated from corresponding HG modes. The HG mode shown here are imaged after nontilted cylindrical lenses. (b) ALG modes generated from pure HG$_{5,5}$ and HG$_{10,10}$ modes. The central peak is typical of ALG$_{p,0}$ modes.

99%. Furthermore, in order to confirm the intensity fit procedure with respect to the results of Refs. [24,26], we converted these HG modes into ALG modes using a simple combination of two cylindrical lenses [64–66]. In fact, HG modes form a complete sets of solutions on which any propagation mode can be decomposed. Interestingly, 45° tilted $\mathrm{HG}_{m,n}$ modes have the same decomposition on the straight HG modes set as the $\mathrm{ALG}_{\min(m,n),m-n}$ modes except for a multiple of $\pi/2$ phase for each term [67]. When the 45° tilted mode crosses two identical cylindrical lenses placed around its waist, with the conditions $f = \sqrt{2}d$ and $z_R = f + d$ (f is the focal length of the lenses, d is the distance separating them, and z_R is the Rayleigh range of the impinging mode), each term of the decomposition on the straight modes set accumulates a Gouy phase shift corresponding to the required multiple of $\pi/2$ allowing the conversion of the 45° tilted HG mode to the corresponding ALG mode [65]. In Fig. 13(a), we show different ALG modes generated from a HG modes using this technique. In Fig. 13(b), both $\mathrm{ALG}_{5,0}$ and $\mathrm{ALG}_{10,0}$ generated from pure $\mathrm{HG}_{5,5}$ and $\mathrm{HG}_{10,10}$ modes are displayed. When the intensity profile fit is applied to these ALG modes, similar results (99% and 97%) were obtained. However, their actual purity is expected not to be higher than the one of the corresponding HG modes measured by the diagnosis cavity which lies below 95%. Hence, the purity upper limit given by the fit of the intensity profile appears to be irrelevant.

VII. CONCLUSION

We experimentally demonstrated the transformation of the fundamental TEM_{00} mode to higher-order HG laser modes as high as $\mathrm{HG}_{25,25}$ via a liquid crystal SLM. The generated $\mathrm{HG}_{5,5}/\mathrm{HG}_{10,10}/\mathrm{HG}_{15,15}$ modes were filtered via a two-mirror mode cleaner cavity. The measured conversion efficiencies were 6.6%/3.7%/1.7% for the $\mathrm{HG}_{5,5}/\mathrm{HG}_{10,10}/\mathrm{HG}_{15,15}$ modes. We also demonstrated that $\mathrm{HG}_{m,n}$ modes are compatible with triangular three-mirror cavities used in GW detectors. We then used a triangular cavity to analyze the generated HG modes and found mode purity of 96%/93%/78%, respectively.

Whereas three-mirror cavities accommodate pure, rather slightly astigmatic, HG eigenmodes, linear two-mirror cavities suffer from mode pseudodegeneracy related to mirror aberration. In comparison to ALG modes, HG modes exhibit the advantage of being insensitive to the mirrors' astigmatism provided these are properly angled to the impinging mode. This was verified by simulations as well as theoretical calculations using realistic Virgo mirror surface maps. Our results thus pave the way for further investigations on HG modes for the reduction of thermal noise in optical cavities. Such a thermal noise reduction could be critical for the performance of third generation GW detectors, such as the proposed Einstein Telescope [9,10] or Cosmic Explorer [11,12].

Using a HG mode in GW detectors faces the problem of its generation efficiency. Although there is a scope for it to be improved up to few tens of %, this would require (i) a higher laser power than initially planned for third generation GW detectors using the fundamental modes (ii) a SLM able to stand such a high power (current record 200 W for computer controlled SLM [68]). Other methods such as coherent amplifying network [69] shall definitely be explored.

Also, angling the mirrors requires a prior accurate measurement of their imperfection maps after being coated. Since the mirror has a specific shape for monolithic suspension purposes the manufacturing procedure (polishing, coating, measurement) is to be reconsidered.

ACKNOWLEDGMENTS

We gratefully thank Laurence Pruvost and Remi Soulard for interesting discussions. This work was funded by Agence Nationale de la Recherche (ANR) (ANR-09-BLAN-0207) and Labex First-TF.

APPENDIX A: LEMMAS' PROOFS

Lemma 1.—$Z_0^0(r,\theta)$ is constant and $\mathrm{HG}_{5,5}$ and $\mathrm{HG}_{5+q,5-q}$ ($q \neq 0$) are orthogonal. $\gamma_q^{0,0}$ is then equal to zero.

Lemma 2.—We switch to Cartesian coordinates (x,y). We assign the index $(++)$ to all spatial integrals limited to the quadrant $(x>0, y>0)$, $(-+)$ to the quadrant $(x<0, y>0)$, $(+-)$ to the quadrant $(x>0, y<0)$, and $(--)$ to the quadrant $(x<0, y<0)$. Simple symmetry considerations give

$$\begin{aligned}
\theta(-x,y) &= \pi - \theta(x,y),\\
\theta(x,-y) &= -\theta(x,y),\\
\cos((2l+1)\theta(-x,y)) &= -\cos((2l+1)\theta(x,y)),\\
\cos((2l+1)\theta(x,-y)) &= \cos((2l+1)\theta(x,y)),\\
\sin((2l+1)\theta(-x,y)) &= \sin((2l+1)\theta(x,y)),\\
\sin((2l+1)\theta(x,-y)) &= -\sin((2l+1)\theta(x,y)).
\end{aligned}$$

Equivalently, for q odd,

$$\begin{aligned}
HG_{5+q,5-q}(-x,y) &= HG_{5+q,5-q}(x,y),\\
HG_{5+q,5-q}(x,-y) &= HG_{5+q,5-q}(x,y),
\end{aligned} \tag{A1}$$

and for $q=0$ and q even,

$$\begin{aligned}
HG_{5+q,5-q}(-x,y) &= -HG_{5+q,5-q}(x,y),\\
HG_{5+q,5-q}(x,-y) &= -HG_{5+q,5-q}(x,y).
\end{aligned} \tag{A2}$$

We then infer for q odd, N odd, M odd, and $M \geq 0$

$$\gamma^{N,M}_{q,-+} = \gamma^{N,M}_{q,++} \qquad \gamma^{N,M}_{q,+-} = -\gamma^{N,M}_{q,++} \qquad \gamma^{N,M}_{q,--} = -\gamma^{N,M}_{q,++},$$

so

$$\gamma^{N,M}_{q} = \gamma^{N,M}_{q,++} + \gamma^{N,M}_{q,-+} + \gamma^{N,M}_{q,+-} + \gamma^{N,M}_{q,--} = 0. \tag{A3}$$

Likewise, for q odd, N odd, M odd, and $M < 0$:

$$\gamma^{N,M}_{q,-+} = -\gamma^{N,M}_{q,++} \qquad \gamma^{N,M}_{q,+-} = \gamma^{N,M}_{q,++} \qquad \gamma^{N,M}_{q,--} = -\gamma^{N,M}_{q,++},$$

so $\gamma^{N,M}_{q} = 0$. For q even, N odd, M odd, and $M \geq 0$:

$$\gamma^{N,M}_{q,-+} = -\gamma^{N,M}_{q,+,+} \qquad \gamma^{N,M}_{q,+-} = \gamma^{N,M}_{q,++} \qquad \gamma^{N,M}_{q,--} = -\gamma^{N,M}_{q,++},$$

so $\gamma^{N,M}_{q} = 0$. Finally, for q even, N odd, M odd, and $M < 0$:

$$\gamma^{N,M}_{q,-+} = \gamma^{N,M}_{q,+,+} \qquad \gamma^{N,M}_{q,+-} = -\gamma^{N,M}_{q,++} \qquad \gamma^{N,M}_{q,--} = -\gamma^{N,M}_{q,++},$$

and $\gamma^{N,M}_{q} = 0$. We conclude that for N odd, $\gamma^{N,M}_{q} = 0$.

Lemma 3.—With the same kind of symmetry considerations, we obtain the following:

$$\begin{aligned}
\cos(2l\theta(-x,y)) &= \cos(2l\theta(x,y)),\\
\cos(2l\theta(x,-y)) &= \cos(2l\theta(x,y)),\\
\sin(2l\theta(-x,y)) &= -\sin(2l\theta(x,y)),\\
\sin(2l\theta(x,-y)) &= -\sin(2l\theta(x,y)).
\end{aligned}$$

Using Eqs. (A1) and (A2), we get for q odd and $M \geq 0$:

$$\gamma^{N,M}_{q,-+} = -\gamma^{N,M}_{q,+,+} \qquad \gamma^{N,M}_{q,+-} = -\gamma^{N,M}_{q,++} \qquad \gamma^{N,M}_{q,--} = \gamma^{N,M}_{q,++}$$

so $\gamma^{N,M}_{q} = 0$. Likewise, for q even and $M < 0$:

$$\gamma^{N,M}_{q,-+} = -\gamma^{N,M}_{q,+,+}, \qquad \gamma^{N,M}_{q,+-} = -\gamma^{N,M}_{q,++}, \qquad \gamma^{N,M}_{q,--} = \gamma^{N,M}_{q,++},$$

and $\gamma^{N,M}_{q} = 0$.

Lemma 4.—We define the $\pi/2$ rotation symmetry $\mathbf{R}$ which gives $\mathbf{R}[(x,y)]=(-y,x)$ and $\theta(\mathbf{R}[(x,y)])=\theta(x,y)+\pi/2$. We then have

$$\begin{aligned}
\cos(2l\theta(\mathbf{R}[x,y])) &= (-1)^l \cos(2l\theta(x,y)),\\
\sin(2l\theta(\mathbf{R}[x,y])) &= (-1)^l \sin(2l\theta(x,y)).
\end{aligned}$$

For q even we have:

$$HG_{5+q,5-q}(\mathbf{R}[(x,y)]) = -HG_{5-q,5+q}(\mathbf{R}[(x,y)]),$$

and for q odd:

$$HG_{5+q,5-q}(\mathbf{R}[(x,y)]) = HG_{5-q,5+q}(\mathbf{R}[(x,y)]).$$

Applying these identities to the integral (7) for $l = M/2$ proves the lemma statement.

Lemma 5.—For $-5 \leq q \leq 5$, the $\mathrm{HG}_{5+q,5-q}(x,y)$ mode is given by

$$\begin{aligned}
HG_{5+q,5-q}(x,y) = \mathscr{C}_{5+q,5-q} H_{5+q}\left(\sqrt{2}\frac{x}{w}\right)\\
\times H_{5-q}\left(\sqrt{2}\frac{y}{w}\right) e^{-\frac{x^2+y^2}{w^2}},
\end{aligned} \tag{A4}$$

where H_l is the Hermite polynomial of order l and $\mathscr{C}_{5+q,5-q}$ is a constant. By substituting the variables $X = \sqrt{2}x/w$ and $Y = \sqrt{2}y/w$, the coupling coefficient $\gamma^{N,M}_{q}$ becomes

$$\begin{aligned}
\gamma^{N,M}_{q} \propto \iint_{X^2+Y^2 \leq \frac{2R^2}{w^2}} dX dY \times Z^M_N(X,Y)\\
\times H_5(X) H_{5+q}(X) e^{-X^2} \times H_5(Y) H_{5-q}(Y) e^{-Y^2}.
\end{aligned} \tag{A5}$$

Given the cavity conditions considered above $\sqrt{2}R/w \simeq 7.8$ so the integrals can be extended to infinity thanks to the Gaussian term. Keeping the Cartesian coordinates, Zernike polynomials can be written as [70,71]

$$Z^M_N(X,Y) = \sum_{J=0}^{J_{\max}} \sum_{I=0}^{N-2J} A_{N,M} \times X^I \times Y^{N-2J-I} \tag{A6}$$

The last expression injected into the integral in Eq. (A5) gives

$$\begin{aligned}
\gamma^{N,M}_{q} \propto \sum_{J=0}^{J_{\max}} \sum_{I=0}^{N-2J} A_{N,M} \int_{-\infty}^{+\infty} dX\, H_5(X) H_{5+q}(X) X^I e^{-X^2}\\
\times \int_{-\infty}^{+\infty} dY\, H_5(Y) H_{5-q}(Y) Y^{N-2J-I} e^{-Y^2}.
\end{aligned} \tag{A7}$$

Hermite polynomials admit the recursive relation [72]:

$$H_{l+1}(\xi) = 2\xi H_l(\xi) - 2l H_{l-1}(\xi) \tag{A8}$$

from which one infers that $\xi^j H_l(\xi)$ can be decomposed on a set of Hermite polynomials $H_{l'}(\xi)$ with $l' \leq l + j$. Therefore, using the Hermite polynomials orthogonality

$$\int_{-\infty}^{+\infty} d\xi H_l(\xi) H_{l'}(\xi) e^{-\xi^2} = \sqrt{\pi} 2^l l! \delta_{l,l'}, \tag{A9}$$

the only nonzero terms of the discrete sum in Eq. (A7) corresponds to both conditions $5 + I \geq 5 + q$ and $5-q+N-2J-I \geq 5$, or $q \leq I \leq N - 2J - q$. This implies that q must satisfy $2q \leq N-2J$. Since $\min(J) = 0$, $2q \leq N$ in order to have at least a nonzero term in the sum of Eq. (A7) (assuming the corresponding factor $A_{N,M}$ to be nonzero). In other words, $\gamma^{N,M}_{q} = 0$ for $N < 2q$.

APPENDIX B: GENERATION ALGORITHM OF HG MODES

The Gerchberg-Saxton algorithm was initially designed to reshape the phase of a wave in a given plane knowing both its module and the module of its Fourier transform. This algorithm is naturally applicable in Fourier optics where the issue is to determine the phase that a diffractive optical element, the SLM in this case, applies on an incident beam with a known shape to obtain the required image in the focal plane of the Fourier lens (the diffractive optical element is placed in the object plane of the Fourier lens in order to avoid an additional curved wave front). The Gerchberg-Saxton algorithm goes iteratively back and forth between the object plane where the intensity is imposed by the reading beam and the image plane in which the intensity must have the required distribution, by applying either a Fourier or an inverse Fourier transform. On each iteration, the obtained intensity profile is substituted by the imposed or the required one depending on the considered plane. In these conditions, the phase of the diffracted wave in the Fourier plane is of no interest. This represents a mandatory degree of freedom to determine the required phase map, otherwise the corresponding mathematical problem is too constrained and no solution exists in the general case. When it comes to the generation of a HG propagation mode, both phase and amplitude are defined. In order to release the constraint in the image plane, the mode definition is only applied in a restricted area (named HG area) defined beforehand, whereas the rest of the plane (named noise or free area) is left free. The purity of the HG mode is guaranteed even in a restricted area since it has a Gaussian tail. The algorithm is initialized by choosing a random phase map and constructing the near field $\mathrm{E}_{\mathrm{in}}(x,y)$ with the Gaussian amplitude $|\mathrm{TEM}_{00}(x,y)|$. Then, each iteration is based on the following procedure which is summarized in Fig 14:

(i) The wave field in the image plane is computed using an FFT algorithm:

$$\mathrm{E}_{\mathrm{out}}(X,Y)=\mathcal{F}[\mathrm{E}_{\mathrm{in}}(x,y)].$$

(ii) In the HG area, the field is replaced by the HG mode while keeping the same energy

$$\mathrm{E}'_{\mathrm{out}}=\alpha_{\mathrm{HGarea}}\times\mathrm{HG}_{\mathrm{norm}}(X,Y),\qquad(\mathrm{A10})$$

where α_{HGarea} is the energy of $\mathrm{E}_{\mathrm{out}}$ in the HG area and $\mathrm{HG}_{\mathrm{norm}}(X,Y)$ is the normalized HG mode field restricted to the same area. The field in the noise area remains the same.

(iii) The wave in the object plane is computed using an inverse FFT algorithm.

$$\mathrm{E'}_{\mathrm{in}}(x,y)=\mathcal{F}^{-1}[\mathrm{E'}_{\mathrm{out}}(X,Y)].\qquad(\mathrm{A11})$$

(iv) The amplitude of the near field is replaced by TEM_{00}. The SLM phase map is given by the complex argument of $\mathrm{E'}_{\mathrm{in}}$:

$$\varphi_{\mathrm{SLM}}(x,y)=\mathrm{Arg}[\mathrm{E'}_{\mathrm{in}}(x,y)].\qquad(\mathrm{A12})$$

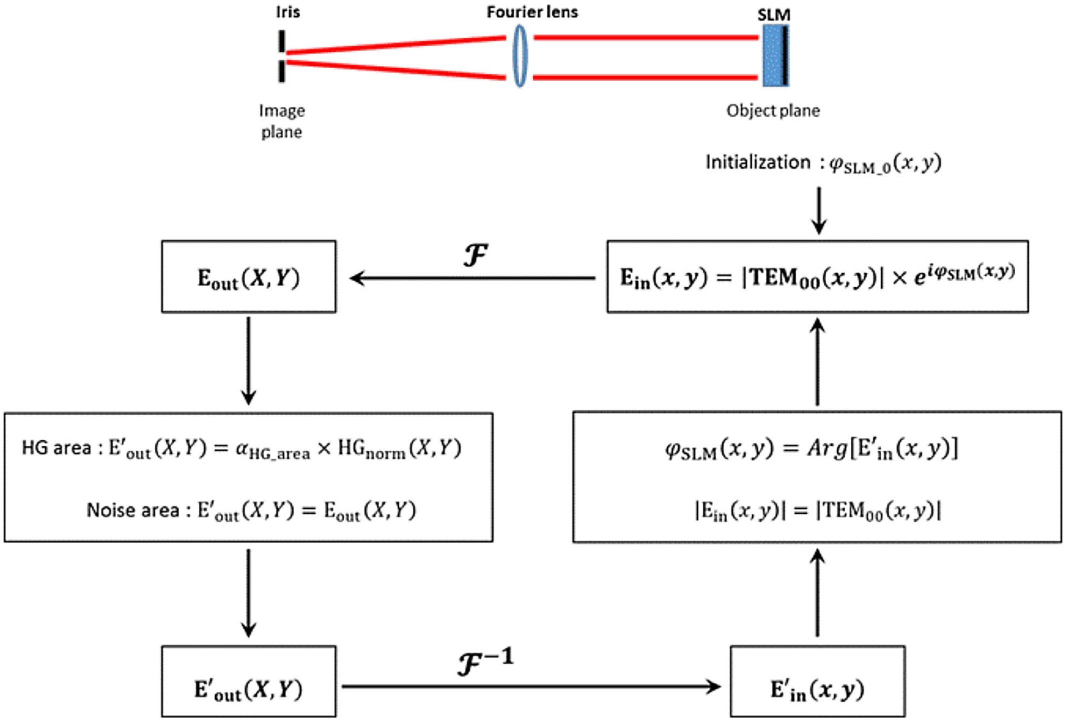

FIG. 14. Graphical illustration of the modified Gerchberg-Saxton algorithm for the generation of HG modes.

For each iteration k, the error is defined as the sum of the fraction of energy in the HG area that is not in the HG mode and the standard deviation of the normalized intensity in the object plane:

$$\mathcal{E}_k = \left[1 - \frac{\left(\iint_{\text{HG area}} \text{HG}_{\text{norm}} \times E^*_{\text{out},k}\right)^2}{\alpha_{\text{HGarea},k}}\right] \tag{A13}$$

$$+\left(\iint (|E'_{\text{in},k}|^2 - |\text{TEM}_{00}|^2)^2\right)^{1/2}. \tag{A14}$$

It decreases with each iteration. In iterative Fourier transform algorithms, vortex stagnation issues might occur that correspond to a very slow convergence or its absence. Relaxation parameters can be introduced to the algorithm to speed up its convergence. However, 20 iterations are sufficient to bring the error below 1% which is satisfactory since the HG mode is targeted to be injected into the mode cleaner cavity. Thus, no study on the vortex stagnation effect upon the algorithm convergence [73] with respect to the initial phase map was conducted. Nevertheless, relaxation parameters were tested but no improvement was observed [74]. The energy conversion efficiency defined as the ratio of the energy of the field energy in the HG area to the energy of the impinging TEM_{00} was also computed. It spreads from 45% for the $\text{HG}_{5,5}$ mode to 20% for the $\text{HG}_{15,15}$ mode. We used a MATLAB program for the iterative calculation of the phase map. Several parameters for the input mode and the output mode had to be defined in the program. The input parameters were the beam width impinging on the SLM surface and the ellipticity of the mode. The output parameters included the values for the mode orders l and m, the ellipticity as well as the waist size of the generated HG mode and the two waists (for the x and y axes) position along the beam propagation direction. The size of the HG mode as well as the size of the HG area were chosen as a trade-off between the purity of the mode, its energy, and the finite size of the SLM pixels. Finally, a blazed grating was added in order to obtain a free diffraction area from unwanted light (undiffracted and diffracted in the free area).

---

[1] A. E. Siegman, *Lasers* (University Science Books, Sausalito, 1986).

[2] K. Numata, A. Kemery, and J. Camp, Thermal-Noise Limit in the Frequency Stabilization of Lasers with Rigid Cavities, Phys. Rev. Lett. **93**, 250602 (2004).

[3] D. G. Matei, T. Legero, S. Häfner, C. Grebing, R. Weyrich, W. Zhang, L. Sonderhouse, J. M. Robinson, J. Ye, F. Riehle, and U. Sterr, 1.5 μm Lasers with Sub-10 MHz Linewidth, Phys. Rev. Lett. **118**, 263202 (2017).

[4] J. Aasi *et al.* (LIGO Scientific Collaboration), Advanced LIGO, Classical Quantum Gravity **32**, 074001 (2015).

[5] F. Acernese *et al.* (VIRGO Collaboration), Advanced Virgo: A second-generation interferometric gravitational wave detector, Classical Quantum Gravity **32**, 024001 (2015).

[6] Y. Aso, Y. Michimura, K. Somiya, M. Ando, O. Miyakawa, T. Sekiguchi, D. Tatsumi, and H. Yamamoto (The KAGRA Collaboration), Interferometer design of the kagra gravitational wave detector, Phys. Rev. D **88**, 043007 (2013).

[7] G. M. Harry, A. M. Gretarsson, P. R. Saulson, S. E. Kittelberger, S. D. Penn, W. J. Startin, S. Rowan, M. M. Fejer, D. R. M. Crooks, G. Cagnoli, J. Hough, and N. Nakagawa, Thermal noise in interferometric gravitational wave detectors due to dielectric optical coatings, Classical Quantum Gravity **19**, 897 (2002).

[8] LIGO Scientific Collaboration, Advanced LIGO, Classical Quantum Gravity **32**, 074001 (2015).

[9] The Einstein Telescope design team, The Einstein telescope: A third-generation gravitational wave observatory, Classical Quantum Gravity **27**, 194002 (2010).

[10] M. Punturo *et al.*, The Einstein telescope: A third-generation gravitational wave observatory, Classical Quantum Gravity **27**, 194002 (2010).

[11] B. P. Abbott *et al.*, Exploring the sensitivity of next generation gravitational wave detectors, Classical Quantum Gravity **34**, 044001 (2017).

[12] D. Reitze *et al.*, The US program in ground-based gravitational wave science: Contribution from the LIGO Laboratory, Bull. Am. Astron. Soc. **51**, 141 (2019).

[13] B. Shapiro, R. X. Adhikari, O. Aguiar, E. Bonilla, D. Fan, L. Gan, I. Gomez, S. Khandelwal, B. Lantz, T. MacDonald, and D. Madden-Fong, Cryogenically cooled ultra low vibration silicon mirrors for gravitational wave observatories, Cryogenics **81**, 83 (2017).

[14] T. Akutsu *et al.* (KAGRA Collaboration), First cryogenic test operation of underground km-scale gravitational-wave observatory KAGRA, Classical Quantum Gravity **36**, 165008 (2019).

[15] E. D'Ambrosio, Nonspherical mirrors to reduce thermoelastic noise in advanced gravitational wave interferometers, Phys. Rev. D **67**, 102004 (2003).

[16] E. D'Ambrosio, R. O'Shaugnessy, K. Thorne, P. Willems, S. Strigin, and S. Vyatchanin, Advanced LIGO: Non-Gaussian beams, Classical Quantum Gravity **21**, S867 (2004).

[17] R. O'Shaughnessy, S. Strigin, and S. Vyatchanin, The implications of Mexican-hat mirrors: Calculations of thermoelastic noise and interferometer sensitivity to perturbation for the Mexican-hat-mirror proposal for advanced LIGO, arXiv:gr-qc/0409050.

[18] E. D'Ambrosio, R. O'Shaughnessy, S. Strigin, K. S. Thorne, and S. Vyatchanin, Reducing thermoelastic noise in gravitational-wave interferometers by flattening the light beams, arXiv:gr-qc/0409075.

[19] J.-Y. Vinet, Mirror thermal noise in flat-beam cavities for advanced gravitational wave interferometers, Classical Quantum Gravity **22**, 1395 (2005).

[20] J.-Y. Vinet, Thermal noise in advanced gravitational wave interferometric antennas: A comparison between arbitrary order Hermite and Laguerre Gaussian modes, Phys. Rev. D **82**, 042003 (2010).

[21] B. Mours, E. Tournefier, and J.-Y. Vinet, Thermal noise reduction in interferometric gravitational wave antennas: Using high order TEM modes, Classical Quantum Gravity **23**, 5777 (2006).

[22] N. Hinkley, J. A. Sherman, N. B. Phillips, M. Schioppo, N. D. Lemke, K. Beloy, M. Pizzocaro, C. W. Oates, and A. D. Ludlow, An atomic clock with 10^{-18} instability, Science **341**, 1215 (2013).

[23] X. Y. Zeng, Y. X. Ye, X. H. Shi, Z. Y. Wang, K. Deng, J. Zhang, and Z. H. Lu, Thermal-noise-limited higher-order mode locking of a reference cavity, Opt. Lett. **43**, 1690 (2018).

[24] M. Granata, C. Buy, R. Ward, and M. Barsuglia, Higher-Order Laguerre-Gauss Mode Generation and Interferometry for Gravitational Wave Detectors, Phys. Rev. Lett. **105**, 231102 (2010).

[25] A. Gatto, M. Tacca, F. Kéfélian, C. Buy, and M. Barsuglia, Fabry-Pérot-Michelson interferometer using higher-order Laguerre-Gauss modes, Phys. Rev. D **90**, 122011 (2014).

[26] P. Fulda, K. Kokeyama, S. Chelkowski, and A. Freise, Experimental demonstration of higher-order Laguerre-Gauss mode interferometry, Phys. Rev. D **82**, 012002 (2010).

[27] C. Bond, P. Fulda, L. Carbone, K. Kokeyama, and A. Freise, Higher order Laguerre-Gauss mode degeneracy in realistic, high finesse cavities, Phys. Rev. D **84**, 102002 (2011).

[28] A. Allocca, A. Gatto, M. Tacca, R. A. Day, M. Barsuglia, G. Pillant, C. Buy, and G. Vajente, Higher-order Laguerre-Gauss interferometry for gravitational-wave detectors with in situ mirror defects compensation, Phys. Rev. D **92**, 102002 (2015).

[29] L. Carbone, C. Bogan, P. Fulda, A. Freise, and B. Willke, Generation of High-Purity Higher-Order Laguerre-Gauss Beams at High Laser Power, Phys. Rev. Lett. **110**, 251101 (2013).

[30] S. Chelkowski, S.Hild, and A. Freise, Prospects of higher-order Laguerre-Gauss modes in future gravitational wave detectors, Phys. Rev. D **79**, 122002 (2009).

[31] T. Hong, J. Miller, H. Yamamoto, Y. Chen, and R. Adhikari, Effects of mirror aberrations on Laguerre-Gaussian beams in interferometric gravitational-wave detectors, Phys. Rev. D **84**, 102001 (2011).

[32] B. Sorazu, P. J. Fulda, B. W. Barr, A. S. Bell, C. Bond, L. Carbone, A. Freise, S. Hild, S. H. Huttner, and J. Macarthur, Experimental test of higher-order LaguerreGauss modes in the 10 m Glasgow prototype interferometer, Classical Quantum Gravity **30**, 035004 (2013).

[33] A. Noack, C. Bogan, and B. Willke, Higher-order LaguerreGauss modes in (non-) planar four-mirror cavities for future gravitational wave detectors, Opt. Lett. **42**, 751 (2017).

[34] J.-Y. Vinet, On special optical modes and thermal issues in advanced gravitational wave interferometric detectors, Living Rev. Relativity **12**, 5 (2009).

[35] F. Bondu, P. Hello, and J.-Y. Vinet, Thermal noise in mirrors of interferometric gravitational wave antennas, Phys. Lett. A **246**, 227 (1998).

[36] Y. T. Liu and K. S. Thorne, Thermoelastic noise and homogeneous thermal noise in finite sized gravitational-wave test masses, Phys. Rev. D **62**, 122002 (2000).

[37] Y. Levin, Internal thermal noise in the LIGO test masses: A direct approach, Phys. Rev. D **57**, 659 (1998).

[38] J.-Y. Vinet, Reducing thermal effects in mirrors of advanced gravitational wave interferometric detectors, Classical Quantum Gravity **24**, 3897 (2007).

[39] The Virgo Collaboration, Measurement of the optical parameters of the virgo interferometer, Appl. Opt. **46**, 3466 (2007).

[40] J. Degallaix, OSCAR a MATLAB based optical FFT code, J. Phys. Conf. Ser. **228**, 012021 (2010).

[41] J. Degallaix, C. Michel, B. Sassolas, A. Allocca, G. Cagnoli, L. Balzarini, V. Dolique, R. Flaminio, D. Forest, M. Granata, B. Lagrange, N. Straniero, J. Teillon, and L. Pinard, Large and extremely low loss: The unique challenges of gravitational wave mirrors, J. Opt. Soc. Am. A **36**, C85 (2019).

[42] J. Degallaix, OSCAR: A MATLAB based package to simulate realistic optical cavities, SoftwareX **12**, 100587 (2020).

[43] M. Born and E. Wolf, *Principles of Optics: Electromagnetic Theory of Propagation, Interference and Diffraction of Light (7th Edition)*, 7th ed. (Cambridge University Press, Cambridge, England, 1999).

[44] A. Duparré, J. Ferre-Borrull, S. Gliech, G. Notni, J. Steinert, and J. M. Bennett, Surface characterization techniques for determining the root-mean-square roughness and power spectral densities of optical components, Appl. Opt. **41**, 154 (2002).

[45] T. Pertermann, J. Hartung, M. Beier, M. Trost, S. Schröder, S. Risse, R. Eberhardt, A. Tünnermann, and H. Gross, Angular resolved power spectral density analysis for improving mirror manufacturing, Appl. Opt. **57**, 8692 (2018).

[46] R. Bonnand, The Advanced Virgo gravitational wave detector: Study of the optical design and development of the mirrors, Theses, Université Claude Bernard—Lyon I, 2012.

[47] N. Matsumoto, T. Ando, T. Inoue, Y. Ohtake, N. Fukuchi, and T. Hara, Generation of high-quality higher-order Laguerre-Gaussian beams using liquid-crystal-on-silicon spatial light modulators, J. Opt. Soc. Am. A **25**, 1642 (2008).

[48] T. Inoue, H. Tanaka, N. Fukuchi, M. Takumi, N. Matsumoto, T. Hara, N. Yoshida, Y. Igasaki, and Y. Kobayashi, LCOS spatial light modulator controlled by 12-bit signals for optical phase-only modulation, in Proc. SPIE Int. Soc. Opt. Eng., Vol. **6487**, edited by L.-C. Chien (2007), p. 64870Y.

[49] T. Ando, Y. Ohtake, N. Matsumoto, T. Inoue, and N. Fukuchi, Generated via complex-amplitude modulation using, Opt. Lett. **34**, 34 (2009).

[50] Y. Ohtake, T. Ando, N. Fukuchi, N. Matsumoto, H. Ito, and T. Hara, Universal generation of higher-order multiringed laguerre-gaussian beams by using a spatial light modulator, Opt. Lett. **32**, 1411 (2007).

[51] D. P. Rhodes, D. M. Gherardi, J. Livesey, D. McGloin, H. Melville, T. Freegarde, and K. Dholakia, Atom guiding along high order Laguerre-Gaussian light beams formed by spatial light modulation, J. Mod. Opt. **53**, 547 (2006).

[52] F. K. Fatemi and M. Bashkansky, Generation of hollow beams by using a binary spatial light modulator, Opt. Lett. **31**, 864 (2006).

[53] M. Mestre, F. Diry, B. Viaris de Lesegno, and L. Pruvost, Cold atom guidance by a holographically-generated Laguerre-Gaussian laser mode, Eur. Phys. J. D **57**, 87 (2010).

[54] V. Carrat, C. Cabrera-Gutiérrez, M. Jacquey, J. W. Tabosa, B. Viaris de Lesegno, and L. Pruvost, Long-distance channeling of cold atoms exiting a 2D magneto-optical trap by a Laguerre-Gaussian laser beam, Opt. Lett. **39**, 719 (2014).

[55] V. S. Pavelyev, V. A. Soifer, M. Duparre, R. Kowarschik, B. Ludge, and B. Kley, Iterative calculation, manufacture and investigation of DOE forming unimodal complex distribution, Opt. Lasers Eng. **29**, 269 (1998).

[56] M. R. Duparre, V. S. Pavelyev, B. Luedge, E.-B. Kley, V. A. Soifer, and R. M. Kowarschik, Generation, superposition, and separation of Gauss-Hermite modes by means of DOEs, 1998.

[57] R. W. Gerchberg and W. O. Saxton, A practical algorithm for the determination of phase from image and diffraction plane pictures, Optik (Stuttgart) **35**, 237 (1972).

[58] F. Nogrette, H. Labuhn, S. Ravets, D. Barredo, L. Béguin, A. Vernier, T. Lahaye, and A. Browaeys, Single-Atom Trapping in Holographic 2D Arrays of Microtraps with Arbitrary Geometries, Phys. Rev. X **4**, 021034 (2014).

[59] M. Pasienski and B. DeMarco, A high-accuracy algorithm for designing arbitrary holographic atom traps, Opt. Express **16**, 2176 (2008).

[60] R. W. P. Drever, J. L. Hall, F. V. Kowalski, J. Hough, G. M. Ford, A. J. Munley, and H. Ward, Laser phase and frequency stabilization using an optical resonator, Appl. Phys. B **31**, 97 (1983).

[61] S. A. Collins and Daniel T. M. Davis, Modes in a triangular ring optical resonator, Appl. Opt. **3**, 1314 (1964).

[62] B. Willke, N. Uehara, E. K. Gustafson, R. L. Byer, P. J. King, S. U. Seel, and R. L. Savage, Spatial and temporal filtering of a 10-W Nd:YAG laser with a Fabry–Perot ring-cavity premode cleaner, Opt. Lett. **23**, 1704 (1998).

[63] S. Goßler, M. M. Casey, A. Freise, A. Grant, H. Grote, G. Heinzel, M. Heurs, M. E. Husman, K. Ktter, V. Leonhardt, H. Lck, M. Malec, K. Mossavi, S. Nagano, P. W. McNamara, M. V. Plissi, V. Quetschke, D. I. Robertson, N. A. Robertson, A. Rdiger, R. Schilling, K. D. Skeldon, K. A. Strain, C. I. Torrie, H. Ward, U. Weiland, B. Willke, W. Winkler, J. Hough, and K. Danzmann, Mode-cleaning and injection optics of the gravitational-wave detector GEO600, Rev. Sci. Instrum. **74**, 3787 (2003).

[64] C. Tamm and C. O. Weiss, Bistability and optical switching of spatial patterns in a laser, J. Opt. Soc. Am. B **7**, 1034 (1990).

[65] M. W. Beijersbergen, L. Allen, H. E. L. O. van der Veen, and J. P. Woerdman, Astigmatic laser mode converters and transfer of orbital angular momentum, Opt. Commun. **96**, 123 (1993).

[66] M. Padgett, J. Arlt, N. Simpson, and L. Allen, An experiment to observe the intensity and phase structure of LaguerreGaussian laser modes, Am. J. Phys. **64**, 77 (1996).

[67] E. Abramochkin and V. Volostnikov, Beam transformations and nontransformed beams, Opt. Commun. **83**, 123 (1991).

[68] https://www.santec.com/en/products/components/slm/.

[69] I. Fsaifes, L. Daniault, S. Bellanger, M. Veinhard, J. Bourderionnet, C. Larat, E. Lallier, E. Durand, A. Brignon, and J.-C. Chanteloup, Coherent beam combining of 61 femtosecond fiber amplifiers, Opt. Express **28**, 20152 (2020).

[70] M. Carpio and D. Malacara, Closed cartesian representation of the Zernike polynomials, Opt. Commun. **110**, 514 (1994).

[71] V. Lakshminarayanan and A. Fleck, Zernike polynomials: A guide, J. Mod. Opt. **58**, 545 (2011).

[72] M. Abramowitz and I. A. Stegun, *Handbook of Mathematical Functions with Formulas, Graphs, and Mathematical Tables*, ninth dover printing, tenth gpo printing ed. (Dover, New York, 1964).

[73] P. Senthilkumaran, F. Wyrowski, and H. Schimmel, Vortex stagnation problem in iterative Fourier transform algorithms, Opt. Lasers Eng. **43**, 43 (2005).

[74] A. Levi and H. Stark, Image restoration by the method of generalized projections with application to restoration from magnitude, J. Opt. Soc. Am. A **1**, 932 (1984).